

Noise cancellation with phase-detection technique for pump-probe measurement and application to stimulated Raman imaging

Keisuke Seto,^{1,2,*} Toshiaki Tsukada,³ Yoshinao Okuda,⁴ Eiji Tokunaga,⁴ and Takayoshi Kobayashi^{1,2,5,6}

¹Advanced Ultrafast Laser Research Center and Department of Engineering Science, University of Electro-Communications, Chofu, Tokyo 182-8585, Japan

²JST, CREST, 5 Sanbancho, Chiyoda-ku, Tokyo 102-0075, Japan

³Keisoku Solution Co., Ltd., Haitsu enomoto B1F, 3-32-18, Nukuikitamachi, Koganei-shi, Tokyo 184-0015, Japan

⁴Department of Physics, Faculty of Science, Tokyo University of Science, 1-3 Kagurazaka, Shinjuku-ku, Tokyo 162-8601, Japan

⁵Department of Electrophysics, National Chiao-Tung University, 1001 Ta Hsueh Rd., Hsinchu 300, Taiwan

⁶Institute of Laser Engineering, Osaka University, 2-6 Yamada-oka, Suita, Osaka 565-0971, Japan

*Corresponding author: seto@ils.uec.ac.jp

Received December 18, 2014; revised February 7, 2015; accepted March 4, 2015;
posted March 4, 2015 (Doc. ID 226620); published April 21, 2015

Intensity noise on a probe beam is a serious obstacle to highly sensitive and high-speed pump-probe microscopy. In this report, a reference beam of the probe is prepared and delayed. The intensity modulation by the sample is measured as the phase modulation of the superposition of detected electrical signals of the probe and reference beams, and the intensity noise is canceled. We evaluate performance of the noise cancellation using the supercontinuum light from a piece of photonic crystal fiber, and find that the noise is canceled by ~26 dB. We then apply the method to a stimulated Raman microscope. This method contributes to highly sensitive and high-speed pump-probe imaging with various light sources. © 2015 Optical Society of America

OCIS codes: (170.0110) Imaging systems; (170.3010) Image reconstruction techniques; (170.3660) Light propagation in tissues.

<http://dx.doi.org/10.1364/JOSAA.32.000809>

1. INTRODUCTION

Various types of pump-probe microscopies such as stimulated Raman scattering (SRS) [1–11], stimulated emission [12–15], and photo-thermal [15–20] microscopies have been investigated to achieve super-resolution with high sensitivity and high-speed imaging. In pump-probe microscopy, a pump beam is irradiated on a sample as a stimulus, and a probe beam is irradiated to detect the stimulation effects. The signal is obtained as the intensity modulation of the probe beam induced by the stimulation on the background of the beam. While the optical source noise is multiplicative to the signal and noise is dominated by the shot noise in the cases of observation of light-emitting effects such as fluorescence and spontaneous Raman, the intensity noise of the probe beam is also additionally included in pump-probe measurements, as it is not factored by the modulation depth of the signal. For example, 1×10^{-4} of the intensity fluctuation of the source deteriorates the signal-to-noise ratio (SNR) by 1×10^{-4} through the multiplicative effect, while it degrades the SNR to 1 for 1×10^{-4} of the modulation depth through the additive effect. Hence, the stability of the background signal of the probe beam is critical in pump-probe microscopy. Lock-in detection is frequently applied to reject the intensity noise of the probe beam as much as possible [21–23]. In this detection scheme, the pump intensity is modulated at a specific frequency, and the intensity modulation of the probe beam around this frequency is detected. The intensity noise apart from the frequency is rejected, thereby

enhancing the SNR. Additionally, a substantial contribution from noise components at some frequencies is rejected by setting the lock-in frequency at an appropriate level to avoid these frequencies. For example, a contribution from the acoustic noise at a low frequency is rejected by a high-frequency lock-in detection in an MHz region. However, noises independent of frequency such as the thermal noise of a load resistor for a photodetector, shot noise of the light source, and white intensity noise of the light source are not rejected by the lock-in detection at any lock-in frequency. The contribution by the thermal noise is reduced with a resonant circuit as a load impedance with a combination of the high impedance and response speed [24]. However, the intensity noise of the light source is irrelevant to the thermal noise, and thus, the intensity noise cannot be reduced by the resonator. In this case, the use of a narrow bandwidth efficiently rejects any noise from nearby frequencies. The bandwidth of frequency measurement is determined by the time constant, and the bandwidth is made narrower by using a longer time constant. Although a narrow bandwidth enhances the SNR inversely proportionally to its bandwidth, it decreases the response speed. Therefore, a lock-in detection scheme involves a trade-off between the SNR and response speed.

To overcome this trade-off problem, we present the following method for the detection of the phase modulation in the detected signal, rather than the intensity modulation, of which physical quantity is common to the intensity noise. We split an

intensity modulated probe beam (e.g., pulsed beam) with a frequency of ω_c into two beams. One beam overlaps with the pump beam, and the other is delayed by a quarter of the intensity modulation cycle. The phase of the former beam coincides with that of the pump beam, forming an “in-phase beam.” The phase of the latter is displaced by 90° , forming a “quadrature beam.” When the in-phase and pump beams are transmitted through a sample, the intensity of the in-phase beam is modulated. The in-phase beam is then detected after being superposed on the quadrature beam. By capturing this superposed beam as a “carrier” of the phase-amplitude modulation, the instantaneous amplitude is determined by the root of the square sum of the intensities of the in-phase and quadrature beams, while the instantaneous phase is the ratio between the two beam intensities. The instantaneous phase of the modulated carrier is represented as $\omega_c t + \theta + \theta_m(t)$, where θ and $\theta_m(t)$ are the initial phase and phase deviation, respectively. The intensity modulation of only the in-phase beam causes a modulation of the ratio between the in-phase and quadrature beams, and hence, this intensity modulation creates the phase deviation, $\theta_m(t)$ [Fig. 1(a)]. In this scheme, because the in-phase and quadrature beams are generated from the same light source, the instantaneous amplitudes of the in-phase and quadrature beams are common. Thus, the intensity ratio or phase deviation is not affected by the variation of the instantaneous amplitude of the carrier induced by intensity noise of the light source [Fig. 1(b)]. Therefore, through the phase detection of the carrier beam, the intensity noise of the source is canceled, while the signal of the sample is detected independently of the intensity noise.

Because this noise cancellation does not limit the band, the aforementioned trade-off is principally removed. In realizing this scheme, the crosstalk between the phase deviation and instantaneous amplitude of the carrier in the phase detection must be removed to prevent the intensity noise from being detected as phase noise. To fulfill this requirement, we introduce a method for detecting the phase deviation independently of the instantaneous amplitude.

In this study, we apply the present method to SRS microscopy. Pulsed beams with higher and lower photon energies are used in the SRS experiment. When the difference in their energy coincides with a vibrational energy of a molecule, a photon of the higher energy is annihilated and the counterpart

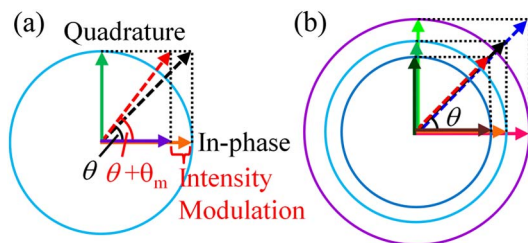


Fig. 1. Principle of the phase-detected pump-probe measurement displayed in a complex plane. (a) The orange, purple, and green arrows indicate the in-phase beam without intensity modulation by the sample, the in-phase beam with intensity modulation, and the quadrature beam, respectively. The black and red dotted arrows indicate the carrier beam (superposition of the in-phase and quadrature beams) with and without the intensity modulation by the sample being excited by the pump. θ and θ_m indicate the initial phase and phase deviation of the carrier, respectively. (b) The effect of a light source intensity change. The radii of the circles indicate the intensity of the light source or the instantaneous amplitude of the carrier.

is created in the SRS process. The typical modulation depth of the beam intensity in this process has been reported to be in the range of 10^{-3} to 10^{-5} in microscopy [2,4,9,10]. By sweeping the beams or translating a sample, the intensity modulation signal of the beams provides an image of the molecular vibration of the sample without labeling [2,3]. In this study, a titanium-sapphire laser oscillator generates the beam of the lower photon energy. The beam of the higher photon energy is prepared in the form of a white pulsed beam by supercontinuum generation with the same light source and a photonic crystal fiber (PCF) [25]. In PCFs, supercontinuum generation is possible even with the low peak power of the input pulse since the tight confinement of the input beam in a core surrounded by air voids results in a large amount of nonlinearity. In the present paper, the beam of the lower photon energy serves as the pump beam, and the white beam serves as the probe (or carrier) beam. In the present SRS microscopy scheme, the pump and probe beams from the common light source render the synchronization of plural sources unnecessary. Furthermore, we readily conduct spectral imaging through the spectral dispersion of the white probe beam [26,27]. However, the intensity noise of the white beam with the PCF is substantially high [28–32], causing a serious problem when the PCFs are applied to high-speed pump-probe microscopy. This cannot be solved by simply using high-frequency lock-in detection since this noise is nearly white, even in a megahertz frequency region [29–32]. Therefore, we demonstrate the feasibility of applying the present method to pump-probe imaging with the use of a continuum and extending the capability of light source choices through noise rejection.

2. OPTICS

Figure 2 illustrates the optics system for an SRS microscope with phase-sensitive detection. The optics system is similar to that in our previous works [26,33]. A titanium-sapphire laser (Mira 900P, COHERENT) generates the 76.3 MHz optical pulse repetition. The pulse duration is 2.5 ps, and the center wavelength is set at 802 nm. This beam is split into probe and pump arms. In the probe arm, the polarization angle is adjusted by a half-wave plate, and then coupled into a 1 m length PCF (NL-2.3-790-2, THORLABS) with a zero-dispersion wavelength (ZDW) of 790 nm by a microscope objective lens ($\times 40$, NA = 0.65) to generate a white-light continuum. The spectral bandwidth is preferred to be a requisite minimum at certain conversion efficiency into the white light to maximize spectral power density. The input power tends to be more distributed in shorter wavelength components with a PCF of a shorter ZDW at a certain length of the PCF [25]. Hence, a PCF with a ZDW of 790 nm, which is closer to the input wavelength than the 750 nm in the previous work [33], is selected. In addition, the length is increased to 1 m from 30 cm in the previous work [33] to enhance conversion efficiency. The spectral power density is increased by ~ 10 times higher than that in the previous work. The efficiency of the white-light generation also depends on the polarization angle of the input pulse due to small birefringence in the PCF. Hence, the polarization angle is adjusted to maximize the efficiency.

A microscope objective lens ($\times 40$, NA = 0.65) collimates the generated white light, and a Glan-Thompson polarizer adjusts and fixes the polarization angle. A polarization beam

splitter (PBS) divides the white pulse beam into the in-phase and quadrature arms. The splitting ratio is adjusted by the polarization angle determined by the polarizer. Fixation of the polarization angle is critically important for the cancellation of the optical noise in the white-light source. The polarization angle of the white pulse beam fluctuates from pulse to pulse. The polarization angle must be fixed before the beam splitter to reduce the fluctuation in the splitting ratio. Otherwise, this fluctuation would result in the phase fluctuation of the carrier. In the quadrature arm, the beam is delayed for a quarter cycle of the pulse repetition by a 98 cm additional optical path, and prepared as the quadrature beam. The in-phase and quadrature beams are spatially overlapped and aligned collinearly with each other on another PBS, and function as the carrier beam. A notch filter (NF808-34, THORLABS) rejects the spectral component near the 802 nm input beam. The spectra of the in-phase and quadrature beams cover 600–780 nm [Fig. 2(b)]. This spectral bandwidth of $\sim 4200 \text{ cm}^{-1}$ is enough for most of the molecular vibrations used in SRS microscopy.

In the pump arm, the pulse beam is guided through the delay stage to adjust the timing so that it temporally overlaps with only the in-phase pulse beam. The pump beam is chopped at 4.48 kHz, and then spatially overlapped and aligned collinearly with the carrier beam on the notch filter. The beams are sent to a microscope and focused on a sample by a microscope objective ($\times 10$, NA = 0.25 or $\times 40$, NA = 0.85). In SRS imaging, the sample is scanned by piezo actuators on a stage (NanoMax300, THORLABS). The beams transmitted through the sample are collected and collimated through a condenser lens. A notch filter (NF808-34, THORLABS) rejects the spectral component of the pump beam at the level of

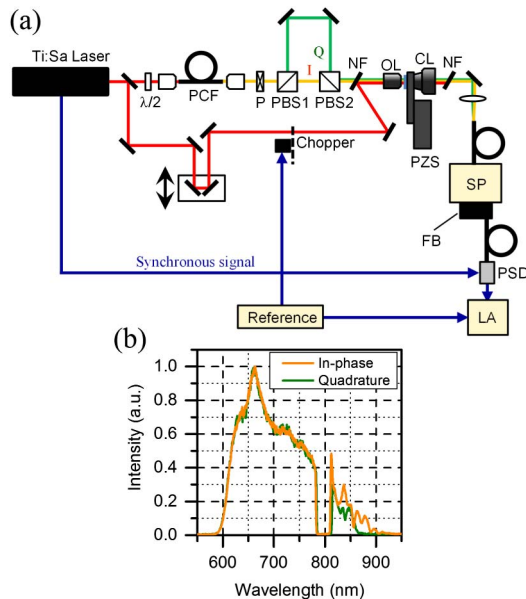


Fig. 2. Optics system of a stimulated Raman microscope with (a) present phase-sensitive detection, and (b) spectra of in-phase and quadrature beams. (a) The red, orange, green, and blue lines indicate 802 nm, in-phase, quadrature pulse beams, and electrical signal flows, respectively. $\lambda/2$, half-wave plate; PCF, photonic crystal fiber; P, Glan-Thompson polarizer; PBSs, polarization beam splitters; I, in-phase beam; Q, quadrature beam; NF, notch filter; OL, objective lens; CL, condenser lens; PZS, piezo stage; SP, spectrometer; FB, fiber bundle; PSD, present phase-sensitive detector; and LA, lock-in amplifier.

55 dB. The carrier beam is guided into a spectrometer (SpectraPro-300i, ACTON) by a piece of optical fiber. The focal length and F number of the spectrometer are 30 cm and 4, respectively. The groove density on the grating, blaze wavelength, and line dispersion are 300 grooves/mm, 500 nm, and 10.8 nm/mm, respectively. The spectrum of the carrier is imaged on the entrance facet of a 128×16 fiber bundle (core/clad: 100/110 μm). The bundle splits the spectrum into 128 components, and 16 fibers of the same spectral component are bundled. The bundle of 16 fibers guides a spectral component into a developed phase-sensitive detector (PSD), which is described in detail in the following section. The optical pulse from the laser oscillator is detected with a fast photodiode to generate the synchronous signal for the phase-sensitive detection. The output signal from the PSD is lock-in detected at the chopping frequency.

3. COMPOSITION OF PHASE SENSITIVE DETECTOR

The circuit block diagram of the PSD is shown in Fig. 3(a). The in-phase and quadrature beams are detected by an avalanche photodiode [referred to as APD in Fig. 3(a)]. The photocurrent signals of the in-phase and quadrature beams are multiplied with the APD. The multiplication is needed to detect low-intensity beams and suppress noise effects caused by the subsequent circuit. Then the photocurrent around the carrier frequency is converted into a voltage signal by a parallel resonant circuit (RES). This voltage signal is buffered and amplified by a preamplifier (PA) with a high input impedance. This configuration contributes to the suppression of the thermal noise contribution owing to a high load impedance of the RES while maintaining the required response speed [24]. Then the voltage signal is multiplied by the synchronous signal of the light source with a multiplier (ML), to obtain an error

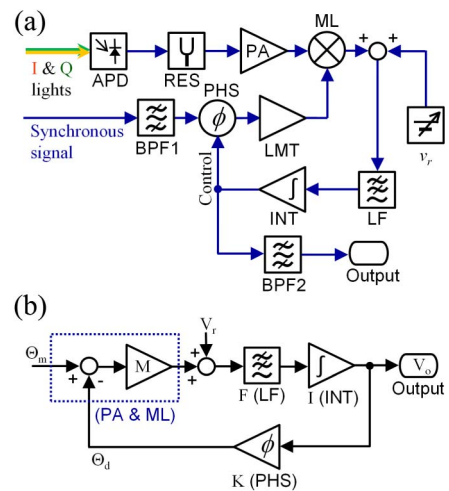


Fig. 3. (a) Circuit block diagram of the present phase-sensitive detector. (b) Block diagram of the phase feedback control. APD, avalanche photodiode; RES, resonator of carrier frequency; PA, pre-amplifier; ML, multiplier; BPFs, bandpass filters; PHS, phase shifter; LMT, amplitude limiter; v_r , bias voltage source for offset; LF, loop filter; INT, integrator; Θ_m , Θ_d , V_r , and V_o : Laplace transformations of the phase deviation of the carrier signal [$\theta_m(t)$], the phase deviation of the synchronous signal [$\theta_d(t)$], the offset voltage (v_r), and the output signal ($v_o(t)$), respectively; M: response function of the combined gain of the multiplier and pre-amplifier; F, I, and K: response functions of the loop filter, integrator, and phase shifter, respectively.

signal for a feedback control of a phase deviation of the synchronous signal.

The synchronous signal from the light source is filtered by a bandpass filter (BPF1) to obtain the fundamental component. A phase deviation is applied on this signal in a phase shifter (PHS). The phase deviation is controlled by a feedback signal based on the abovementioned error signal to track the deviation on the optical signal. The amplitude is fixed by a limiter (LMT) for the sake of simplicity of the design, and sent to the ML. An offset (v_r) is added to the output (the error signal) from the ML to adjust the phase difference between the optical signal and the synchronous signal. This v_r contains an unintentional offset caused by the electrical components. The unintentional offset can be compensated for by an intentional offset. This signal is integrated by an integrator (INT) through a loop-filter (LF), such as a low-pass filter. Then the integrated signal controls the phase deviation of the synchronous signal to track the phase deviation of the optical signal. The LF compensates for an inappropriate removal of a high-frequency component in the error signal by the INT. Therefore, it enables a high-speed feedback. In this configuration, the control signal is proportional to the phase deviation with an offset of the phase difference. This signal is transmitted through a bandpass filter (BPF2), and observed with the lock-in amplifier. Owing to the lock-in detection of the output through the BPF2, dynamic range is enhanced by eliminating a direct current offset and unwanted noise in the high-frequency range.

We use an APD of S5343, HAMAMATSU as a photodetector. Then, the photocurrent is converted to a voltage signal by the RES. This signal is buffered with a non-inverting amplifier (functions as the PA) based on an operation amplifier (LMH6624) of $\times 5.3$ voltage gain. This voltage signal is amplified by 20 dB with a transistor (2SC3356)-based amplifier and input into a multiplier device (AD835) (functions as the ML).

In the arm of the synchronous signal, it is amplified by 20 dB by a narrow-band amplifier based on a field-effect transistor (FET) (2SK241). Its bandwidth is 10 MHz and it functions as the BPF1. Then the signal is sent to a voltage controlled phase shifter, or all-pass filter (functions as the PHS) based on an operation amplifier (LMH6609) and variable-capacitance diode (BB148). The phase deviation of the synchronous signal is controlled by a feedback bias voltage signal on the variable-capacitance diode. The synchronous signal is then converted into a square wave by a digital comparator based on ADCMP600 to maintain the amplitude at constant (i.e., LMT), and input into the ML.

The v_r is adjusted with the applied voltage on the summing input terminal of the AD835. The LF is a third-order Bessel type low-pass filter of 3 MHz cutoff frequency based on the LMH6609. The INT is an integrator circuit of 0.16 μ s integration time based on the LMH6609. The integrated signal for the feedback control is divaricated and filtered through a bandpass filter (functions as the BPF2) and output. The BPF2 is composed of a second-order Butterworth type high-pass filter of 400 Hz cutoff frequency and a second-order Butterworth type low-pass filter of 100 kHz cutoff frequency with 20 dB gain.

Note, the present configuration is similar to our previous report [26] to observe the difference signal between the probe beam and a reference beam from the same light source of the probe. In [26], the optical signal is multiplied by the synchronous signal, and its phase deviation is feedback controlled,

based on the low-frequency component in the multiplied signal. However, the present and previous ones are different in the following way. The output positions in the diagrams and the purposes of the feedbacks are different from each other. In the previous work, the output is obtained just after the ML through a low-pass filter to obtain the difference signal of the probe and reference beams, while it is the feedback signal itself in the present circuit to observe the phase deviation of the synchronous signal, which tracks the deviation of the optical signal. The different function of the feedback creates a difference in the response speed. In the previous work, the function of the feedback is compensation for the difference in the transmissions for the probe and reference beams, and thus, the feedback response frequency must be set lower than the modulation frequency of the pump beam so as not to cancel the signal. Hence it is set at 65 Hz for 4.48 kHz modulation frequency. In the present work, it must be set higher than the modulation frequency to track the phase deviation on the carrier. As mentioned later, the response frequency is set at 32 kHz.

4. OPERATION PRINCIPLE

The working principle is based on our previous work [26]. In the previous work, the difference between the probe and reference signals (corresponding to the in-phase and quadrature signals, respectively) is observed. The gains for the signals are determined by the phase deviation of the synchronous signal. Then the phase deviation is feedback controlled to cancel the difference with a response speed slow enough not to respond to the intensity modulation of the probe signal by the sample. The background signal, including the intensity noise but excluding the modulation signal, is canceled in the difference signal. In the present PSD, the feedback scheme similar to that in [26] is operated, but the response is faster to cancel also the intensity modulation of the in-phase signal by the sample. In this configuration, the phase deviation of the synchronous signal is controlled so that its instantaneous phase is always perpendicular to that of the optical signal (carrier). The signal for control of the phase deviation, but neither the carrier nor synchronous signal, is observed. The modulation of this control signal is proportional to the phase modulation of the carrier, as the control signal swings to force the instantaneous phase of the synchronous signal to track that of the carrier signal at a 90° interval.

Because the phase of the quadrature beam is delayed by 90° against the in-phase beam, the fundamental component of the quadrature beam is expressed as a sine wave when that of the in-phase beam is expressed as a cosine wave. The splitting ratio of the white pulse beam into the in-phase and quadrature beams is expressed as $a:b$ ($a + b = 1$). Thus, the in-phase signal is given as

$$a\{1 + m(t)\}A(t) \cos(\omega_c t), \quad (1)$$

and the quadrature signal is

$$b'A\left(t - \frac{T}{4}\right) \sin(\omega_c t). \quad (2)$$

Here, $A(t)$ is the instantaneous amplitude and is proportional to the intensity of the light source, including amplitude noise;

$m(t)$ is the amplitude modulation of the signal on the in-phase beam; ω_c is the carrier frequency; and T is the carrier cycle.

When the in-phase and quadrature beams are the pulse beams, their optical currents from the photodetector are proportional to the following terms, respectively:

$$a \sum_{n=-\infty}^0 A_n \{1 + m(nT)\} \delta(t - nT), \quad (3)$$

and

$$b' \sum_{n=-\infty}^0 A_n \delta\left(t - nT - \frac{T}{4}\right). \quad (4)$$

Here, A_n is the pulse intensity of the n th pulse and $\delta(t)$ is the Dirac's delta function. The Laplace transformations of these currents are

$$a \sum_{n=-\infty}^0 A_n \{1 + m(nT)\} \exp(-snT) \quad (5)$$

and

$$b' \sum_{n=-\infty}^0 A_n \exp\left\{-s\left(n + \frac{1}{4}\right)T\right\}. \quad (6)$$

These optical currents are converted into voltage signals by the thermal noise effect less the RES in the present system.

One might be concerned about the phase change caused by the RES. We describe the effect of the RES as follows. The responses of a inductance L , capacitance C , and resistance R are sL , $1/(sC)$, and R , respectively, and hence the response of the RES is

$$\left(\frac{1}{sL} + sC + \frac{1}{R}\right)^{-1} = \frac{L\omega_0^2 s}{(s + \zeta\omega_0)^2 + (1 - \zeta^2)\omega_0^2}, \quad (7)$$

where ω_0 and ζ are the resonant frequency and damping factor, and determined by the element values, as follows:

$$\omega_0^2 = \frac{1}{LC}, \quad \text{and} \quad 2\zeta = \frac{1}{Q} = \frac{L\omega_0}{R}. \quad (8)$$

This R contains a contribution of unintentional energy losses in the inductor and capacitor. From Eqs. (5) and (7), the voltage signal of the in-phase beam in the time domain is

$$a \frac{L\omega_0^2}{\sqrt{1 - \zeta^2}} \sum_{n=-\infty}^0 A_n \{1 + m(nT)\} \exp\{-\zeta\omega_0(t - nT)\} \times \cos\left\{\sqrt{1 - \zeta^2}\omega_0(t - nT) + \beta\right\}, \quad (9)$$

where

$$\beta = \tan^{-1} \frac{\zeta}{\sqrt{1 - \zeta^2}}. \quad (10)$$

Here, by adjusting the resonant frequency as follows,

$$\sqrt{1 - \zeta^2}\omega_0 = \omega_c, \quad (11)$$

the signal is written as

$$a \left[\frac{L\omega_0^2}{\sqrt{1 - \zeta^2}} \sum_{n=-\infty}^0 A_n \{1 + m(nT)\} \exp\{-\zeta\omega_0(t - nT)\} \right] \times \cos(\omega_c t + \beta). \quad (12)$$

The ζ should be set at a value large enough to observe high-speed phenomena. In other words, the change of $m(t)$ is slower than the damping speed. Hence, $m(t)$ is assumed to be a constant within the time constant of the resonator, and Eq. (12) is approximated in the same form as Eq. (1), where β is set at 0 by adjusting the initial phase of the synchronous signal:

$$a\{1 + m(t)\}A(t) \cos(\omega_c t), \quad (13)$$

where

$$A(t) = \left[\frac{L\omega_0^2}{\sqrt{1 - \zeta^2}} \sum_{n=-\infty}^0 A_n \exp\{-\zeta\omega_0(t - nT)\} \right]. \quad (14)$$

The voltage signal of the quadrature beam is similarly obtained as

$$b' \exp\left(\frac{\zeta\omega_0 T}{4}\right) A(t) \sin(\omega_c t). \quad (15)$$

Therefore, the instantaneous amplitude of the quadrature beam [Eq. (2)] is proportional to that of the in-phase beam, as follows:

$$A\left(t - \frac{T}{4}\right) = \exp\left(\frac{\zeta\omega_0 T}{4}\right) A(t). \quad (16)$$

Note that the instantaneous amplitude is not that of the light source itself but the convolution of it by the resonator. However, this effect does not destroy the correlation between the instantaneous amplitudes of the in-phase and quadrature beams [Eq. (16)], and it allows the following noise cancellation. Hereafter, the quadrature signal is written as follows, for simplicity,

$$bA(t) \sin(\omega_c t), \quad (17)$$

where the damping effect is contained in the optical splitting ratio:

$$b' \exp\left(\frac{\zeta\omega_0 T}{4}\right) = b. \quad (18)$$

The superposition of the in-phase and quadrature signals [Eqs. (13) and (17)],

$$A(t)[a^2\{1 + m(t)\}^2 + b^2]^{1/2} \sin\{\omega_c t + \theta_m(t)\}, \quad (19)$$

is captured as a phase-amplitude-modulated wave and input to the ML. Here, the phase deviation is determined by the ratio

between the instantaneous amplitudes of the in-phase and quadrature signals, as follows:

$$\theta_m(t) = \tan^{-1} \left[\frac{a}{b} \{1 + m(t)\} \right]. \quad (20)$$

Note that this phase deviation is dependent only on $m(t)$ and independent of $A(t)$. The instantaneous amplitude, including the amplitude noise of the light source at any frequency is canceled. When $m(t) \ll 1$,

$$\theta_m(t) \cong \frac{ab}{a^2 + b^2} m(t) + \tan^{-1} \left(\frac{a}{b} \right). \quad (21)$$

The size of phase modulation is approximately proportional to the amplitude modulation only of the in-phase signal.

The synchronous signal around the fundamental component of amplitude D and phase deviation $\theta_d(t)$ is expressed as

$$D \cos\{\omega_c t + \theta_d(t)\}. \quad (22)$$

Here, we assume that $\theta_d(t)$ is designed to be controlled by the output of the INT, $v_o(t)$ as mentioned later, with the following proportionality relation with constant k :

$$\theta_d(t) = k v_o(t). \quad (23)$$

The output from the ML is the product of the carrier and synchronous signals:

$$\begin{aligned} & \frac{1}{2} A(t) D [a^2 \{1 + m(t)\}^2 + b^2]^{1/2} \\ & \times [\sin\{\theta_m(t) - \theta_d(t)\} + \sin\{2\omega_c t + \theta_m(t) + \theta_d(t)\} + \text{HF}(t)]. \end{aligned} \quad (24)$$

Here, $\text{HF}(t)$ refers to the higher frequency components originating in the harmonic components in the square wave by the digital limiter. We then add the offset value of v_r . The LF rejects the high-frequency components containing that at $2\omega_c$. Hence, we focus on the first term in Eq. (24) with v_r :

$$\frac{1}{2} A(t) D [a^2 \{1 + m(t)\}^2 + b^2]^{1/2} \times \sin\{\theta_m(t) - \theta_d(t)\} + v_r. \quad (25)$$

When $\theta_m(t) - \theta_d(t) \ll 1$, this term is approximated as

$$\frac{1}{2} A(t) D [a^2 \{1 + m(t)\}^2 + b^2]^{1/2} \times \{\theta_m(t) - \theta_d(t)\} + v_r. \quad (26)$$

This signal is integrated, and the integrated signal controls $\theta_d(t)$. At the same time, this integrated signal is transmitted through the BPF2 to reject offset and electrical noise. When the observing frequency (ω) is sufficiently lower than $2\omega_c$, the cutoff frequency of the INT can be set to be low enough against $2\omega_c$, and the LF is not required because the high-frequency components are properly rejected by the INT. In other words, the rejection of the high-frequency components by this LF allows the cutoff frequency of the INT to be set at a higher frequency than that without the LF. This enhances the response speed of the feedback loop, and high-speed observation becomes possible.

The present scheme is considered to be a feedback system of $\theta_d(t)$ that tracks $\theta_m(t)$, as described in the block diagram in Fig. 3(b). Based on Eq. (26), the photodetector and the ML are captured as the combination of a subtracter for $\theta_m(t)$ and $\theta_d(t)$, and an amplifier of the gain $M(t)$ in this scheme. Here,

$$M(t) = \frac{1}{2} A(t) D [a^2 \{1 + m(t)\}^2 + b^2]^{1/2}. \quad (27)$$

The response function of this amplifier is defined as $M(s) \cdot V_r$ (the Laplace transformation of v_r) is then added to the signal. The signal is filtered by the LF of response function $F(s)$ and integrated. The response function of this INT with an integration time T is expressed as

$$I(s) = \frac{1}{sT}. \quad (28)$$

This integrated signal controls the PHS of response function $K(=k)$ and provides the output. When $M(t)$ is assumed to be time invariant, i.e., $A(t)$ is constant and $m(t)$ is ignored; this feedback system is considered to be a linear time-invariant system. Hence, $\Theta_d(s)$ is given as follows:

$$\Theta_d(s) = KI(s)F(s)[M\{\Theta_m(s) - \Theta_d(s)\} + V_r], \quad (29)$$

where $\Theta_m(s)$ and $\Theta_d(s)$ are the Laplace transformations of $\theta_m(t)$ and $\theta_d(t)$, respectively. Based on Eq. (29), $\Theta_d(s)$ is calculated as follows:

$$\Theta_d(s) = \frac{1}{\frac{sT}{kF(s)M} + 1} \Theta_m(s) + \frac{1}{\frac{sT}{kF(s)} + M} V_r. \quad (30)$$

Therefore, the final value of θ_d is calculated as follows:

$$\theta_d(\infty) = \lim_{s \rightarrow 0} \{s\Theta_d(s)\} = \theta_m(\infty) + \frac{1}{M} v_r. \quad (31)$$

In Eq. (31), v_r functions as the reference value for the difference between $\theta_m(t)$ and $\theta_d(t)$, and when $v_r = 0$, $\theta_d(t)$ is controlled so that the synchronous signal is perpendicular to the carrier signal. Equation (30) indicates that, when the frequency ω in the observed signal is too high, the system is unable to respond, and results in a large displacement between $\theta_m(t)$ and $\theta_d(t)$. This situation is restated as a shortage of the response speed to detect high-speed phenomena. When the feedback gain is set at a large value (e.g., by setting T as a small value), this effect is compensated and the cutoff frequency of the system can be increased. However, only increase of the gain results in an insufficient rejection of the $2\omega_c$ and $\text{HF}(t)$ components in Eq. (24). This problem is solved by the LF and an adequate rejection of only the high-frequency components. The high cutoff frequency of the feedback is permitted with the high gain. The phase retardation of the feedback loop containing the LF must not exceed 180° at the cutoff frequency; otherwise, the positive feedback would cause the system to oscillate. As a rule of thumb, a maximum compromised retardation between stability and response speed can be found in the range of 120 - 135° .

For the present system, $D = 1$ and the maximum value of A is 1. Then, the maximum gain of the ML is $1/2$, where $a \rightarrow 1$ or

$b \rightarrow 1$. The open-loop response function at the largest gain (the most unstable condition) is

$$KI(s)F(s)M = k \frac{1}{sT} F(s) \frac{1}{2}. \quad (32)$$

The LF is designed as a third-order Bessel-type low-pass filter with a 3 MHz cutoff frequency. Its response function ($F(s)$) is calculated as follows:

$$F(s) = 1.11 \times 10^{23} \times (s^3 + 1.15 \times 10^8 s^2 + 5.65 \times 10^{15} s + 1.11 \times 10^{23})^{-1}. \quad (33)$$

The integration time T is set at 0.16 μ s and the response of the PHS $k = 65.7$ mrad/V. The cutoff frequency is calculated as 32 kHz, and the phase retardation is 92°. The high-frequency component of $2\omega_c$ at 152.6 MHz is suppressed by -185 dB.

$M(t)$ is not time invariant because of the fluctuation of $A(t)$ caused by noise from the light source. Therefore, the requirement of detecting the phase deviation without the optical noise is fulfilled by eliminating the contribution of $M(t)$. Without the time invariance assumption, Eq. (29) is replaced by the following:

$$\Theta_d(s) = KI(s)F(s) \times [M(s) \otimes \{\Theta_m(s) - \Theta_d(s)\} + V_r], \quad (34)$$

where \otimes is the convolution operator. When the deconvolution by M is expressed by $(1/M \otimes)$, Eq. (34) is deduced as follows:

$$(1/M \otimes) \left\{ \frac{sT\Theta_d(s)}{kF(s)} \right\} + \Theta_d(s) = \Theta_m(s) + (1/M \otimes) V_r. \quad (35)$$

Here, when the response speed is high enough (i.e., $|kF(j\omega)/T| \gg \omega$), the first term in the left side of Eq. (35) is ignored:

$$\Theta_d(s) = \Theta_m(s) + (1/M \otimes) V_r. \quad (36)$$

Based on Eq. (36), when $v_r = 0$, the effect of $M(t)$ is rejected. $\theta_d(t)$ is deduced as follows:

$$\theta_d(t) = \theta_m(t) \quad \text{or} \quad v_o(t) = \frac{\theta_m(t)}{k}. \quad (37)$$

Regardless of the values of $A(t)$, a , and b , the synchronous signal is perpendicular to the carrier signal. Therefore, the optical noise is canceled, but the output $v_o(t)$ is proportional to the carrier phase deviation at any optical splitting ratio. Therefore, to achieve the maximum noise cancellation with this scheme, it is important to control the instantaneous phase of the synchronous signal perpendicular to that of the carrier signal.

Finally, we mention the case for a light source of intensity modulated continuous wave (CW). From Eqs. (1) and (2), the phase deviation with the CW light source is

$$\theta_m(t) = \tan^{-1} \left[\frac{aA(t)}{b'A(t - \frac{T}{4})} \{1 + m(t)\} \right]. \quad (38)$$

Therefore, the phase noise caused by the light source originates in an uncorrelated nature between $A(t)$ and $A(t - T/4)$.

We define the spectra of these terms as $\tilde{A}_I(\omega)$ and $\tilde{A}_Q(\omega)$, respectively. Here,

$$\begin{aligned} \tilde{A}_Q(\omega) &= \exp\left(-j\omega \frac{T}{4}\right) \tilde{A}_I(\omega) \\ &= \tilde{A}_I(\omega) + \left\{ \exp\left(-j\omega \frac{T}{4}\right) - 1 \right\} \tilde{A}_I(\omega). \end{aligned} \quad (39)$$

The second term in the right side explains the difference in the correlated noise component with the noise component in the in-phase beam, and an addition of the uncorrelated component perpendicular to that of the in-phase beam. The noise not to be canceled is the incoherent summation of this noise at respective frequencies. The power spectrum of this term is

$$\left| \exp\left(-j\omega \frac{T}{4}\right) - 1 \right|^2 |\tilde{A}_I(\omega)|^2. \quad (40)$$

Thus the observed noise with the band of ω_{ob} is

$$\left[\int_{-\omega_{ob}/2}^{\omega_{ob}/2} \left| \exp\left(-j\omega \frac{T}{4}\right) - 1 \right|^2 |\tilde{A}_I(\omega)|^2 d\omega \right]^{\frac{1}{2}}. \quad (41)$$

Here, when the noise is assumed to be white,

$$|\tilde{A}_I(\omega)|^2 = N^2, \quad (42)$$

the noise is calculated as follows:

$$\begin{aligned} &N \left[\int_{-\omega_{ob}/2}^{\omega_{ob}/2} \left| \exp\left(-j\omega \frac{T}{4}\right) - 1 \right|^2 d\omega \right]^{\frac{1}{2}} \\ &= N \left[2\omega_{ob} - \frac{16}{T} \sin\left(\frac{T}{8}\omega_{ob}\right) \right]^{\frac{1}{2}}. \end{aligned} \quad (43)$$

This result is approximated as

$$N \left[2\omega_{ob} - \frac{16}{T} \sin\left(\frac{T}{8}\omega_{ob}\right) \right]^{\frac{1}{2}} \cong \frac{\pi\omega_{ob}}{16\sqrt{3}\omega_c} N \sqrt{\omega_{ob}}, \quad (44)$$

under the assumption of $\omega_c \gg \omega_{ob}$. This result indicates that the factor to the noise without our method ($N\sqrt{\omega_{ob}}$) is $\pi\omega_{ob}/(16\sqrt{3}\omega_c)$, and the noise component in the quadrature signal uncorrelated to the in-phase signal is increased proportionally to the bandwidth; the noise cancellation performance is degraded proportionally to the bandwidth. However, a substantial noise cancellation is still possible with a considerable bandwidth. As an example, when the band is set as $\omega_{ob} = \omega_c/10$, this factor is ~ 0.045 , and ~ 27 dB cancellation is still expected.

5. EXPERIMENT

A. Signal Gain Dependence on Optical Input Power and Splitting Ratio

We investigated the dependence of the output signal intensity of the PSD on the optical input power at the fixed splitting ratio of $a = b$. We adjusted the optical power of the carrier beam using a variable neutral density filter just after the polarizer. The power of the pump beam was fixed at 74 mW, and the maximum power of the carrier beam was 24 mW on the sample. The gain of the APD was fixed. The carrier and pump

beams were focused into the cyclohexane in a 5 mm length cell by a $\times 10$ NA = 0.25 microscope objective lens. We observed the SRS signal of a CH stretching mode of cyclohexane at $2,854\text{ cm}^{-1}$. We set the time constant of the lock-in amplifier at 1 s.

We then investigated the dependence of the signal intensity on the splitting ratio into the in-phase and quadrature beams at a fixed optical power. We set the APD gain as large as possible within less than saturation of the circuit. The polarizer adjusted the splitting ratio.

B. Noise Cancellation Performance on Optical Splitting Ratio

We observed noise spectra of the 802 nm pulsed beam from the laser oscillator and the white beam. We input the beams into a photodiode module (PDA36A-EC, THORLABS) and observed spectra of the output with a spectrum analyzer (DSA815, RIGOL). All wavelength components of the white beam except the 802 nm component were input. The band frequency of the photodiode module ranges from DC to 10 MHz. The bandwidth was set at 300 Hz for the observation of noise spectra. The optical power of the 802 nm pulse from the oscillator was adjusted by a neutral density filter in such a way that the average output power from the photodiode module was equal to that of the white beam.

We evaluated the output noise as the intensity-modulation equivalent value at various optical splitting ratios. First, we measured the intensity modulation of the cyclohexane SRS using the present circuit to obtain the factor between the intensity modulation of the in-phase beam and the output intensity of the phase modulation of the carrier. To observe the intensity modulation of the SRS, we blocked the quadrature beam, fixed the phase of the synchronous signal, and lock-in detected the signal just after the LF with the in-phase and chopped pump beams. In this case, the ML worked only as a down converter, and the output at the LF was proportional to the power of the in-phase beam. Then the signal intensity of the in-phase beam was measured with only the chopped in-phase beam directly inputted. The modulation equivalent intensity of the SRS signal was measured through normalization according to the signal intensity of the directly chopped in-phase beam. Next, the feedback of the phase was set to be active, and the SRS signal intensity was measured on the PSD with the quadrature and chopped pump beams. We determined the modulation depth of the in-phase beam according to the SRS and PSD-detected signal intensity, and obtained the factor between them. We set the time constant of the lock-in detection at 1 s in all of these measurements.

The intensity noise of the in-pulse beam was measured by inputting only a non-chopped in-phase beam and fixing the phase of the synchronous signal according to the preceding method. We set the time constant at 10 ms and measured the noise signals 140 times. We divided the root mean square (RMS) value of the 140 noise signals by 10 to convert it into the unit bandwidth value, and normalized it according to the in-phase beam intensity to calculate the equivalent noise density of the intensity modulation.

The phase noise of the carrier observed on the present PSD was evaluated with the phase feedback by inputting the in-phase and quadrature beams without the pump beam and without chopping. We set the time constant at 10 ms and

measured the noise signals 140 times. We divided the RMS of the 140 values by 10, and then converted it into the intensity modulation equivalent noise density according to the preceding protocol. We repeated the protocol at various splitting ratios, and evaluated the dependency of the noise cancellation on the ratio.

C. Application to SRS Microscopy

We prepared the sample with 4 μm polystyrene (PS) beads dispersed in a polyvinyl alcohol (PVA) film on a glass slide. We captured the SRS image of the $3,054\text{ cm}^{-1}$ Raman band of PS with a $\times 40$ NA = 0.85 objective lens. The pixel size was set at $0.25\ \mu\text{m}$, and the image size was $10 \times 10\ \mu\text{m}$ (41×41 pixels). The powers of the 802 nm pump, in-phase, and quadrature beams were 43, 10, and 10 mW, respectively, at the sample surface. First, we captured the image by modulating the amplitude of the in-phase beam. As detailed in the experiment in Section 5.B, we blocked the quadrature beam, fixed the phase of the synchronous signal, and lock-in detected the signal at just after the LF. Second, we fed the phase back and captured the image through the present PSD with the in-phase and quadrature beams. In both cases, the time constant of the lock-in detection and the dwelling time were set at 100 and 200 ms, respectively.

6. RESULTS AND DISCUSSION

A. Signal Gain Dependence on Optical Input Power and Splitting Ratio

Red plots in Fig. 4(a) show the dependence of the SRS signal intensity on the optical power of the white beam source through the present PSD. The optical input power is the sum of the power of the in-phase and quadrature beams at the APD. The intensity modulation depth of the in-phase beam by SRS is 1.7×10^{-3} . The signal intensity is constant at $\sim 30\text{ mV}$ and independent of the optical power from 1.5 to $8\ \mu\text{W}$, as expected in the phase detection excluding the multiplicative source-intensity effect.

Figure 4(b) explains the dependence of the signal intensity on the optical unbalance between the in-phase and quadrature beams. The optical unbalance is defined by $(I - Q)/(I + Q)$ with the optical powers of the in-phase (I) and quadrature (Q) beams. As in Eq. (21), the gain of $\theta_m(t)$ for $m(t)$ depends

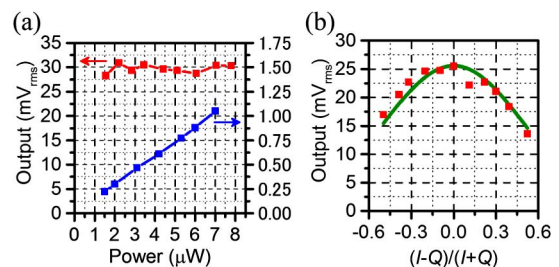


Fig. 4. (a) Dependence of signal intensity of a cyclohexane SRS signal on the optical input power. The red and blue plots indicate the phase detection scheme and the auto-balanced detection scheme in [26], respectively. The input power is the sum of those of the in-phase (probe) and quadrature (reference) beams measured at the APD. (b) Dependence of signal intensity on the intensity unbalance of the in-phase (I) and quadrature (Q) beams. The red plots indicate experimental values, and the green line indicates the theoretical value of the phase-detected pump-probe method.

on the optical splitting ratio, and the gain depends on the optical unbalance as in the following term:

$$\frac{1-x^2}{2(1+x^2)}; \quad x := \frac{I-Q}{I+Q}. \quad (45)$$

The signal should be proportional to the term in Eq. (45) when using the phase-detected pump-probe method. The green line in Fig. 4(b) indicates the fitted curve with the term in Eq. (45) on the experimental data (red plots). In that fitting, only the amplitude is varied. The curve thoroughly explains the signal intensity dependence, as expected in successful phase detection.

B. Noise Cancellation Performance on Optical Splitting Ratio

Figure 5(a) shows noise spectra of the beams in a 0–100 kHz range, and 5(b) shows the same in a 0–10 MHz range. The average output powers of the beams are 4.6 dBm. The noise power of the oscillator overlaps (the red plots) that of the electrical noise of the detection system (the blue plots). The intensity of the beam from the oscillator is stable and the noise is below the detection limit. The noise spectrum of the white beam (the green plots) is observed above the detection limit from DC to 10 MHz, and is independent of frequency, or white. This white noise originates in an amplification of the shot noise of the laser oscillator [31]. Thus, high-frequency lock-in detection to avoid acoustic noise is not effective to attain high SNR for the white beam with PCFs. This fact indicates that an active noise rejection around the observation frequency is required to achieve high SNR.

The intensity noise of the white beam source is $1.1 \times 10^{-4} \text{ Hz}^{-1/2}$ [the pink line in Fig. 5(c)]. In Fig. 5(c), the noise observed through the developed PSD is converted into the intensity modulation equivalent value of the in-phase beam and plotted as red dots. The optical noise is canceled by $\sim 26 \text{ dB}$ (20 times) to $\sim 5 \times 10^{-6} \text{ Hz}^{-1/2}$. The results of the experiments described in Sections 5.A and 5.B clearly explain that the phase modulation of the carrier, rather than the intensity

modulation of the carrier beam, is detected independently of the intensity and/or intensity noise of the carrier. The present scheme demonstrates a successful phase-sensitive detection of signal and intensity noise cancellation.

Certain balanced detection methods [26,33,34,35] offer other ways of cancellation of the optical intensity noise on a probe beam. In these methods, a reference beam is prepared from the same beam source as that of the probe beam, and the detected signal of the reference beam is subtracted from that of the probe beam. The intensity of the pulsed probe beam after measuring the sample is

$$\begin{aligned} & \sum_{n=-\infty}^0 A_n \{1 + m(nt)\} \delta(t - nT) \\ &= \sum_{n=-\infty}^0 A_n m(nt) \delta(t - nT) + \sum_{n=-\infty}^0 A_n \delta(t - nT). \quad (46) \end{aligned}$$

The multiplicative and additive noise components are included in A_n of the first and second terms of the right member, respectively. The balanced detection is intended to cancel only the additive component by the subtraction. The signal intensity versus the probe and reference beam power with the balanced detection of [26] is shown as blue plots in Fig. 4(a). The intensity is proportional to the beam power, which demonstrates that the multiplicative effect to the signal is not canceled. The noise cancellation efficiency is maximized when the signal intensities of the probe and reference beams are equated. When the intensity balance is displaced, the intensity noise is insufficiently or excessively subtracted, and the noise persists depending on the amount of the unbalance [26,33]. In the present phase detection, the multiplicative effect of A_n is canceled, as is shown as the independence of the beam power in Fig. 4(a). The additive noise is also canceled since it is proportional to the multiplicative one [Eq. (46)]. Additionally, because of the cancellation of the multiplicative effect, the noise-rejection performance is principally independent of the intensity balance, as shown in Fig. 5(c). Through this feature, even when the optical balance is displaced during a measurement, the maximized noise cancellation is always maintained. This is especially advantageous for imaging measurement applications, which we describe in detail later. This feature also helps make parallel noise cancellations at plural wavelengths feasible [26,33]. The optical splitting ratios are mismatched because of the dependence of the performance of practical optics such as beam splitters on wavelengths. As a result of this mismatch, when the optical splitting ratio is set so that maximum noise cancellation is attained at a specific wavelength, the noise cancellation performance on the other wavelengths is degraded without the ratios being compensated. In the present method, the performance is independent of the ratio, and the parallel measurement is realized readily with a number of the present PSDs. One might think a combination of the spectrometer and a fast CMOS camera operating in a $\sim \text{MHz}$ readout frequency [36] can be applied as an array of the photodetectors and MLs for this purpose. However, the readout timing (or phase deviation) must be controlled independently for respective pixels in the present method. This operation is difficult with the available CMOS cameras. Thus we use the fiber bundle

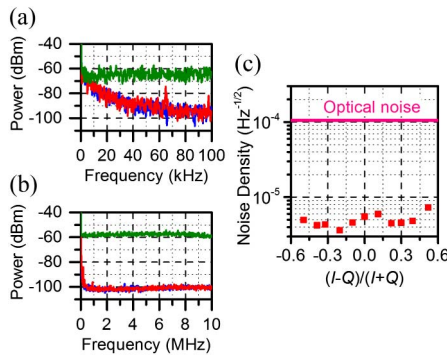


Fig. 5. (a) and (b) Noise spectra of 802 nm pulsed beam from the laser oscillator and white beam source. The blue, red, and green plots indicate electrical noise power of the observation system, noise power of the pulsed beam from the oscillator, and that of the white beam source. (a) The frequency range is 0–100 kHz. (b) The range is 0–10 MHz. (c) Dependence of observed noise on the intensity balance of the I and Q beams, converted to the intensity modulation equivalent noise density. The pink line indicates the intensity noise on the in-phase beam measured at $(I-Q)/(I+Q) = 0$. The red plots indicate the observed noise through the present PSD.

to split the spectrum and input into the PSDs in the present work.

As in usual balanced detection schemes, the noise floor of the present method is determined by the fluctuation of the splitting ratio at the beam splitter. This fluctuation originates in the quantum nature of photons (shot noise). The observed shot-noise current (σ_L) is calculated as follows:

$$\sigma_L = \sqrt{2qI_L F}; \quad I_L = SP, \quad (47)$$

where q , I_L , F , S , and P are the elemental charge, average optical current, bandwidth, photosensitivity, and average optical power, respectively. When larger amounts of photons by ε are distributed into the in-phase arm, the amount of those distributed into the quadrature arm is less distributed by ε . The phase deviation is determined by the ratio of the in-phase and quadrature signals. Thus, the ratio of the in-phase and quadrature beam powers is

$$\frac{I + \varepsilon}{Q - \varepsilon} \cong \frac{I}{Q} \left(1 + \frac{\varepsilon}{I} + \frac{\varepsilon}{Q} \right), \quad (48)$$

when $\varepsilon \ll I$ and Q . Therefore, when the optical splitting ratio is equal ($I = Q$), the shot noise is double that of the in-phase beam.

In the experiment, the optical power of the in-phase beam is $3.5 \mu\text{W}$ at the APD. The S of the APD is 0.42 A/W , and the excessive noise caused by multiplication is negligible because of the small multiplication factor (~ 2 times). Using these parameters, the shot noise is calculated as $9.3 \times 10^{-7} \text{ Hz}^{-1/2}$. The noise caused by the circuit measured without an optical input is $7.6 \times 10^{-7} \text{ Hz}^{-1/2}$. The experimental value is $\sim 5 \times 10^{-6} \text{ Hz}^{-1/2}$ and larger by ~ 5 times. The noise floor of the present equipment is probably determined by the phase noise of the synchronous signal caused by the circuit, since the floor is upraised when the optical signal is input and the phase difference between the optical and synchronous signals is defined. The simple digital comparator converts the sinusoidal wave signal to a square wave by amplitude clipping. The timing when the wave signal crosses the threshold voltage of the comparator is disturbed by the electrical noise on the wave and/or power supply. This process converts the electrical noise in the whole frequency range into phase noise of the synchronous signal. In the near future, we will replace the comparator with an analog auto-gain control circuit as the LMT. Let us compare with our previous work [26] of the auto-balanced scheme with the similar configuration. In [26], the difference is obtained by flipping the sign of either the probe or reference signals through multiplication by the synchronous signal. The gains for the signals are adjusted with the phase deviation. The noise floor in [26] is almost the same value of $\sim 5 \times 10^{-6} \text{ Hz}^{-1/2}$ with similar probe-beam power of $3 \mu\text{W}$. This result is explained by the fluctuation of the gains caused by the phase noise, since the circuit involving the synchronous signal is almost the same. Therefore, the same technical factor determines the noise floor for both schemes although the different physical quantities are observed.

In the present PSD, a common photodetector measures the in-phase and quadrature beams. This scheme helps make measurement feasible via a common spectrometer for the two beams [26]. The noise in the white continuum on one

wavelength is different from that on a different wavelength. Hence, if the beams are detected by different photodetectors, two different spectrometers are required for spectroscopy. The center wavelength and spectral bandwidth must be equated in the two; otherwise, the correlation between the intensities of the two beams is disturbed, resulting in the phase noise of the carrier. Meeting this requirement requires a complex system. However, in the present study, we satisfy this requirement in a simple and robust system using the common spectrometer.

C. Application to SRS Microscopy

Figure 6(a) shows an SRS image obtained by the intensity modulation on the in-phase beam. The modulation equivalent RMS value on the 144 pixels surrounded by the orange square in Fig. 6(a) is calculated as 3.1×10^{-4} . The modulation equivalent noise density is $1.0 \times 10^{-4} \text{ Hz}^{-1/2}$ from this value when the origin of these signals is assumed as noise. This value is almost the same as that of the noise density of the in-phase beam, and it means that these signals originate from the intensity noise of the white beam source. In this image, the intensity noise of the in-phase beam is dominant, and no meaningful structure is captured at this time constant. Figure 6(b) shows an image through the present PSD. The signal intensity is converted into the intensity modulation depth equivalent value of the in-phase beam, and the relative color scale is adjusted as in Fig. 6(a). The fluctuation of the signal is quite small in the film region compared with that in Fig. 6(a) because of noise suppression. A discoid signal distribution with a $4 \mu\text{m}$ diameter corresponding to the PS bead is captured with the modulation equivalent value of $\sim 1.5 \times 10^{-4}$. The RMS value on the 144 pixels surrounded by the square is 2.6×10^{-5} . The noise density is $8.4 \times 10^{-6} \text{ Hz}^{-1/2}$ on the assumption that all contributions to these signals are the intensity noise of the source. This value is near the noise floor of $\sim 5 \times 10^{-6} \text{ Hz}^{-1/2}$ determined by the present circuit configuration, and the noise cancellation to the noise floor is almost achieved in the imaging application. The reason for this larger value may be the offset caused by the cross phase modulation effect [2] on the PVA film. In fact the noise density is obtained as $4.6 \times 10^{-6} \text{ Hz}^{-1/2}$ without the pump beam. Therefore, the intensity noise of the light source is canceled at least to the circuit noise. The detection limit for the present system is determined by the circuit noise. These results confirm the feasibility of applying

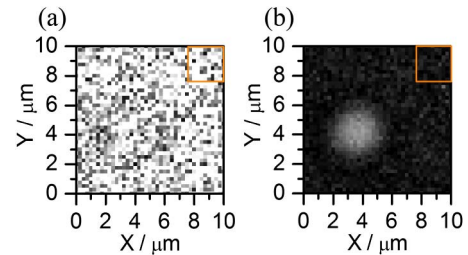


Fig. 6. SRS images on a 3054 cm^{-1} Raman band of a $4 \mu\text{m}$ polystyrene bead embedded in a polyvinyl alcohol film. The orange squares indicate 144 pixels for noise evaluation. The images are constructed on (a) the intensity modulation depth of the in-phase beam and (b) the phase modulation of the carrier. The signal intensity is converted into the equivalent value of the intensity modulation, and the relative color scale is unified with (a).

the method to SRS imaging, with noise cancellation and no suppression of the SRS signal.

The high-speed imaging could not be demonstrated on the present system. It takes 14.5 hours to capture an image of 512×512 pixels with the 200 ms dwelling time. The most important factor preventing the high-speed imaging in this result is the low SNR, which requires the long time constant. The noise is composed of that caused in the circuit and the optical shot noise, and the former one determines the noise floor in the result. The most dominant factor for the circuit noise is the phase noise of the synchronous signal caused in the present amplitude limitation, and this noise is eliminated by modifying the circuit configuration, as described in Section 6.B. The shot noise subsequently limits the SNR. The contribution of the shot noise is hindered with a higher power probe beam. The circuit noise composed of the thermal noise and that by the active devices finally limits the SNR. The contributions of these effects are reduced with an enhanced dynamic range of the circuit to accept the high power probe light without deteriorating the shot noise limited SNR. One of the useful ways is changing the PA with a low noise FET and the active multiplication IC (AD835) into a passive mixer. Then, the observation frequency should be increased with high-frequency modulation of the pump beam and high-frequency lock-in detection. The feedback response speed should be also increased with a shorter time constant of the LF and INT. For instance, the noise density is calculated as $5.5 \times 10^{-8} \text{ Hz}^{-1/2}$ with a power of 1 mW of the in-phase beam. Therefore, SNR = 10 for a SRS signal of 10^{-4} requires a time constant of 30.5 μs , and thus, 61 μs dwelling time is allowed. It takes 16 s for an image of 512×512 pixels.

Here we compare the present method with the usual balanced detection in terms of the factor determining the maximum dwelling speed. When balanced detection is applied in imaging, the optical intensity ratio between the probe and reference beams is disturbed because of the dependence of transmittance on the sample position. To compensate for this effect, a feedback scheme known as auto-balance [13,26,34,37] automatically controls the gain of the reference and/or probe beam. The response speed is preferable to be faster than the dwelling speed in the imaging; otherwise, the auto-balance would not track the transmittance change, resulting in less-than-maximum noise cancellation. The response speed also must be slower than the intensity modulation speed of the signal on the probe beam; otherwise the signal would be eliminated by the feedback. In other words, the signal modulation and auto-balance feedback scheme doubly limit the dwelling speed. As an example, the response frequency of the auto-balance must be 10 times lower than the modulation frequency to observe 90% of the full modulation depth of the signal. The dwelling speed should be half the response to compensate for half the intensity unbalance effect change. Thus, the maximum dwelling speed is determined to be 20 times slower than the modulation speed. Therefore, to perform the high-speed imaging, the modulation frequency is set at a much higher frequency than the dwelling frequency for high feedback cutoff frequency. In a high-speed imaging of 4 μs dwelling time [37], the modulation and cutoff frequencies are set at 10 MHz and 500 kHz, respectively. In the present method, unbalance compensation is not required for the noise cancellation. Although the feedback scheme is used in the

present PSD, the response speed must be higher than the modulation speed of the signal to track the phase deviation. In the present system, the feedback frequency must be 10 times higher than the modulation frequency to detect 90% of the full modulation depth. The dwelling speed is limited by the modulation frequency, as in the lock-in detection scheme.

In addition, having a common circuit in the present PSD for the in-phase and quadrature signals simplifies the high-speed imaging process. In the usual balanced detection, the probe and reference signals are involved in different circuit paths. To apply this scheme to high-speed imaging, the timing difference between inputting the signals into a subtraction circuit should be precisely regulated to maintain the intensity correlation. Hence, the difference in delay and the frequency dependence (dispersion) between the paths is non-negligible. This factor depends on the individual characteristics of the elements, circuit pattern, temperature, and so on, requiring dispersion compensation [37] for individual equipment. In the present PSD, the common path of the signals makes the dispersion automatically common, rendering dispersion compensation unnecessary.

Additionally, let us mention a parallel measurement on a number of wavelengths. According to Refs. [10,11,38], ~ 100 mW average input power with a picosecond pulse is possible for a biological sample. Hence, the parallel measurement on ~ 100 channels is not impossible for the abovementioned condition with ~ 100 mW white light of narrower spectral bandwidth than that in the present work. The quadrature beam can bypass the microscope to avoid damage on the sample. Additionally, such high a power super continuum light source is already realized [39,40] and commercially available [41,42].

We believe the high-speed imaging will be realized on the present scheme through satisfying the abovementioned requirements because of the amplitude noise cancellation in the phase deviation at any frequencies [Eq. (20)] and observation of the deviation independently of the instantaneous amplitude [Eq. (37)].

7. CONCLUSION

In this pump-probe microscopy study, we demonstrate a scheme for detecting a signal as the phase modulation on a periodically intensity modulated carrier beam to reject intensity noise on the probe beam. Contrary to the lock-in detection, the scheme does not resort to band limitation. The source beam is split into in-phase and quadrature beams, which are then overlapped to create the carrier beam. The instantaneous phases of the in-phase and pump beams are made equal, and that of the quadrature beam is made perpendicular to that of the pump beam through an additional optical path. The intensity modulation on the in-phase beam, which is caused by sample measurement, is converted into the phase modulation on the carrier beam. Through this process, the intensity noise on the light source is not converted to the phase modulation, but is canceled, and the SNR is enhanced. This scheme principally enables high-speed measurement because it does not limit the band. The intensity noise is canceled as the multiplicative effect in the present scheme rather than the additive effect to be canceled in the usual balanced detection. Therefore, the maximum noise cancellation is maintained independently of the intensity unbalance between the

in-phase and quadrature beams. This feature contributes to the robustness against the intensity unbalance between the beams caused in the measurement, as well the auto-balanced scheme.

Phase detection without crosstalk with the instantaneous amplitude of the carrier signal is of vital importance when taking this phase-detected pump-probe measurement. Therefore, we develop the PSD to detect the phase deviation of the carrier signal independently of its instantaneous amplitude. In this detection system, we compare the instantaneous phases of the carrier signal and the synchronous signal of the light source by multiplication, and control the phase deviation of the synchronous signal to maintain the phase difference at 90°. We observe that the phase control signal, rather than the carrier or synchronous signals, detects the phase modulation. Maintaining the 90° phase difference is the key to rejecting the intensity noise.

In the present detection system, a common photodetector detects the in-phase and quadrature beams. This configuration permits the use of a common spectrometer for the beams. The common spectrometer guarantees that the beams at the photodetector will have the same center wavelength and spectral bandwidth. Thus, the correlation of the intensity fluctuations is maintained for the beams, even when the scheme is applied to white light, in which case the intensity fluctuation differs depending on wavelength. Parallel measurements at different wavelengths are readily taken with many PSDs. In addition, the in-phase and quadrature signals are involved in the common circuit. This configuration is free of the dispersion difference between the circuits for the signals, and does not destroy the intensity correlation between them. These features help to keep the system simple and robust for high-speed imaging applications, as delicate dispersion compensation is not required. Although the principal noise floor is double that of the shot noise of the in-phase beam, the present noise cancellation cannot achieve such a performance, probably because of the circuit configuration. We believe that the shot noise limited performance is achieved through a modification of the circuit.

We apply the present method to SRS microscopy to demonstrate its feasibility. In this microscopy, the white pulsed beam from a piece of the PCF functions as the carrier beam, and the SRS image is captured on a Raman band through the spectrometer. The present method cancels the significant noise on the white beam and dramatically modifies the SNR of the image. With many PSDs, multi-color or spectral imaging is readily performed because of its high suitability for spectroscopy. The present method allows for multiple simple measurements in highly sensitive and high-speed microscopy by expanding the light source choices.

ACKNOWLEDGMENTS

This work was partially supported by JSPS KAKENHI, Grant Number 26620117. This study was partially supported by a joint research project at the Institute of Laser Engineering, Osaka University, under contract number B1-27. This work was partially financially supported by a Grant-in-Aid for Scientific Research (No. 24740261) received from the Japan Society for the Promotion of Science and a joint research project at the Institute of Laser Engineering, Osaka University, Project number 2014B2-19. This work was partially supported

by the National Science Council of the Republic of China, Taiwan (NSC 98-2112-M-009-001-MY3), and a grant from the Ministry of Education, Aiming for Top University (MOE ATU) Program at National Chiao-Tung University (NCTU).

REFERENCES

1. E. Ploetz, S. Laimgruber, S. Berner, W. Zinth, and P. Gilch, "Femtosecond stimulated Raman microscopy," *Appl. Phys. B* **87**, 389–393 (2007).
2. C. W. Freudiger, W. Min, B. G. Saar, S. Lu, G. R. Holtom, C. He, J. C. Tsai, J. X. Kang, and X. S. Xie, "Label-free biomedical imaging with high sensitivity by stimulated Raman scattering microscopy," *Science* **322**, 1857–1861 (2008).
3. P. Nandakumar, A. Kovalev, and A. Volkmer, "Vibrational imaging based on stimulated Raman scattering microscopy," *New J. Phys.* **11**, 033026 (2009).
4. A. Gambetta, V. Kumar, G. Grancini, D. Polli, R. Ramponi, G. Cerullo, and M. Marangoni, "Fiber-format stimulated-Raman-scattering microscopy from a single laser oscillator," *Opt. Lett.* **35**, 226–228 (2010).
5. Y. Ozeki and K. Itoh, "Stimulated Raman scattering microscopy for live-cell imaging with high contrast and high sensitivity," *Laser Phys.* **20**, 1114–1118 (2010).
6. H. T. Beier, G. D. Noojin, and B. A. Rockwell, "Stimulated Raman scattering using a single femtosecond oscillator with flexibility for imaging and spectral applications," *Opt. Express* **19**, 18885–18892 (2011).
7. D. Fu, F.-K. Lu, X. Zhang, C. Freudiger, D. R. Pernik, G. Holtom, and X. S. Xie, "Quantitative chemical imaging with multiplex stimulated Raman scattering microscopy," *J. Am. Chem. Soc.* **134**, 3623–3626 (2012).
8. F.-K. Lu, M. Ji, D. Fu, X. Ni, C. W. Freudiger, G. Holtom, and X. S. Xie, "Multicolor stimulated Raman scattering microscopy," *Mol. Phys.* **110**, 1927–1932 (2012).
9. E. Ploetz, B. Marx, T. Klein, R. Huber, and P. Gilch, "A 75 MHz light source for femtosecond stimulated Raman microscopy," *Opt. Express* **17**, 18612–18620 (2009).
10. B. G. Saar, C. W. Freudiger, J. Reichman, C. M. Stanley, G. R. Holtom, and X. S. Xie, "Video-rate molecular imaging in vivo with stimulated Raman scattering," *Science* **330**, 1368–1370 (2010).
11. Y. Ozeki, W. Umemura, Y. Otsuka, S. Satoh, H. Hashimoto, K. Sumimura, N. Nishizawa, K. Fukui, and K. Itoh, "High-speed molecular spectral imaging of tissue with stimulated Raman scattering," *Nat. Photonics* **6**, 845–851 (2012).
12. W. Min, S. Lu, S. Chong, R. Roy, G. R. Holtom, and X. S. Xie, "Imaging chromophores with undetectable fluorescence by stimulated emission microscopy," *Nature* **461**, 1105–1109 (2009).
13. J. Miyazaki, H. Tsurui, A. Hayashi-Takagi, H. Kasai, and T. Kobayashi, "Sub-diffraction resolution pump-probe microscopy with shot-noise limited sensitivity using laser diodes," *Opt. Express* **22**, 9024–9032 (2014).
14. W. Min, "Label-free optical imaging of nonfluorescent molecules by stimulated radiation," *Curr. Opin. Chem. Biol.* **15**, 831–837 (2011).
15. J. Miyazaki, K. Kawasumi, and T. Kobayashi, "Resolution improvement in laser diode-based pump-probe microscopy with an annular pupil filter," *Opt. Lett.* **39**, 4219–4222 (2014).
16. E. Tamaki, K. Sato, M. Tokeshi, K. Sato, M. Aihara, and T. Kitamori, "Single-cell analysis by a scanning thermal lens microscope with a microchip: direct monitoring of cytochrome c distribution during apoptosis process," *Anal. Chem.* **74**, 1560–1564 (2002).
17. D. A. Nedosekin, E. I. Galanzha, E. Dervishi, A. S. Biris, and V. P. Zharov, "Super-resolution nonlinear photothermal microscopy," *Small* **10**, 135–142 (2014).
18. A. Gaiduk, P. V. Ruijgrok, M. Yorulmaz, and M. Orrit, "Detection limits in photothermal microscopy," *Chem. Sci.* **1**, 343–350 (2010).
19. S. Arunkarthick, M. M. Bijeesh, G. K. Varier, M. Kowshik, and P. Nandakumar, "Laser scanning photothermal microscopy: fast detection and imaging of gold nanoparticles," *J. Microsc.* **256**, 111–116 (2014).

20. J. Miyazaki, H. Tsurui, K. Kawasumi, and T. Kobayashi, "Optimal detection angle in sub-diffraction resolution photothermal microscopy: application for high sensitivity imaging of biological tissues," *Opt. Express* **22**, 18833–18842 (2014).
21. Y. Ozeki, Y. Kitagawa, K. Sumimura, N. Nishizawa, W. Umemura, S. Kajiyama, K. Fukui, and K. Itoh, "Stimulated Raman scattering microscope with shot noise limited sensitivity using subharmonically synchronized laser pulses," *Opt. Express* **18**, 13708–13719 (2010).
22. A. Owyong and E. D. Jones, "Stimulated Raman spectroscopy using low-power cw lasers," *Opt. Lett.* **1**, 152–154 (1977).
23. A. Owyong, "Sensitivity limitations for CW stimulated Raman spectroscopy," *Opt. Commun.* **22**, 323–328 (1977).
24. M. N. Slipchenko, R. A. Oglesbee, D. Zhang, W. Wu, and J.-X. Cheng, "Heterodyne detected nonlinear optical imaging in a lock-in free manner," *J. Biophotonics* **5**, 801–807 (2012).
25. J. M. Dudley, G. Genty, and S. Coen, "Supercontinuum generation in photonic crystal fiber," *Rev. Mod. Phys.* **78**, 1135–1184 (2006).
26. K. Seto, Y. Okuda, E. Tokunaga, and T. Kobayashi, "Multiplex stimulated Raman imaging with white probe-light from a photonic-crystal fibre and with multi-wavelength balanced detection," *J. Phys. D* **47**, 345401 (2014).
27. K. Seto, Y. Okuda, E. Tokunaga, and T. Kobayashi, "Development of a multiplex stimulated Raman microscope for spectral imaging through multi-channel lock-in detection," *Rev. Sci. Instrum.* **84**, 083705 (2013).
28. U. Møller, S. T. Sørensen, C. Jakobsen, J. Johansen, P. M. Moselund, C. L. Thomsen, and O. Bang, "Power dependence of supercontinuum noise in uniform and tapered PCFs," *Opt. Express* **20**, 2851–2857 (2012).
29. J. N. Ames, S. Ghosh, R. S. Windeler, A. L. Gaeta, and S. T. Cundiff, "Excess noise generation during spectral broadening in a microstructured fiber," *Appl. Phys. B* **77**, 279–284 (2003).
30. N. R. Newbury, B. R. Washburn, K. L. Corwin, and R. S. Windeler, "Noise amplification during supercontinuum generation in microstructure fiber," *Opt. Lett.* **28**, 944–946 (2003).
31. K. L. Corwin, N. R. Newbury, J. M. Dudley, S. Coen, S. A. Diddams, K. Weber, and R. S. Windeler, "Fundamental noise limitations to supercontinuum generation in microstructure fiber," *Phys. Rev. Lett.* **90**, 113904 (2003).
32. K. L. Corwin, N. R. Newbury, J. M. Dudley, S. Coen, S. A. Diddams, B. R. Washburn, K. Weber, and R. S. Windeler, "Fundamental amplitude noise limitations to supercontinuum spectra generated in a microstructured fiber," *Appl. Phys. B* **77**, 269–277 (2003).
33. K. Seto, T. Tsukada, Y. Okuda, E. Tokunaga, and T. Kobayashi, "Development of a balanced detector with biased synchronous detection and application to near shot noise limited noise cancelling of supercontinuum pulse light," *Rev. Sci. Instrum.* **85**, 023702 (2014).
34. P. C. D. Hobbs, "Ultrasensitive laser measurements without tears," *Appl. Opt.* **36**, 903–920 (1997).
35. K. Nose, Y. Ozeki, T. Kishi, K. Sumimura, N. Nishizawa, K. Fukui, Y. Kanematsu, and K. Itoh, "Sensitivity enhancement of fiber-laser-based stimulated Raman scattering microscopy by collinear balanced detection technique," *Opt. Express* **20**, 13958–13965 (2012).
36. W. Rock, M. Bonn, and S. H. Parekh, "Near shot-noise limited hyperspectral stimulated Raman scattering spectroscopy using low energy lasers and a fast CMOS array," *Opt. Express* **21**, 15113–15120 (2013).
37. C. W. Freudiger, W. Yang, G. R. Holtom, N. Peyghambarian, X. S. Xie, and K. Q. Kieu, "Stimulated Raman scattering microscopy with a robust fibre laser source," *Nat. Photonics* **8**, 153–159 (2014).
38. R. Kawakami, K. Sawada, A. Sato, T. Hibi, Y. Kozawa, S. Sato, H. Yokoyama, and T. Nemoto, "Visualizing hippocampal neurons with in vivo two-photon microscopy using a 1030 nm picosecond pulse laser," *Sci. Rep.* **3**, 1014 (2013).
39. M. Seefeldt, A. Heuer, and R. Menzel, "Compact white-light source with an average output power of 2.4 W and 900 nm spectral bandwidth," *Opt. Commun.* **216**, 199–202 (2003).
40. T. Schreiber, J. Limpert, H. Zellmer, A. Tünnermann, and K. P. Hansen, "High average power supercontinuum generation in photonic crystal fibers," *Opt. Commun.* **228**, 71–78 (2003).
41. NKT Photonics, "SuperK EXTREME Supercontinuum White Light Laser Sources," <http://www.nktpotonics.com/superkextreme?cid=7856>.
42. Leukos, "Innovative Optical Systems," <http://www.leukos-systems.com/spip.php?rubrique63>.